

Structure, Spectra, and Rearrangement Mechanism of PH_2F_3 : Revisiting a Classic Problem in Structural Inorganic Chemistry

Sébastien Villaume and Alain Strich*

Laboratoire de Chimie Quantique, UMR 7177 LC3, CNRS/Université Louis Pasteur, 4 rue Blaise Pascal, F-67000 Strasbourg;

S. Ajith Perera* and Rodney J. Bartlett

Quantum Theory Project, Department of Chemistry and Physics, P. O. Box 11845, University of Florida

Received: August 18, 2006; In Final Form: January 9, 2007

The structure, spectra, and rearrangement mechanisms of PH_2F_3 , the first member of the $\text{PH}_n\text{F}_{5-n}$ series and a prototype for molecules that undergo rotational isomerism, have been studied. Aided by the tools developed to compute coupled-cluster (CC) Raman intensities and NMR spin–spin couplings, a full spectroscopic characterization of PH_2F_3 is presented. Moreover, the structures and the energetics of the various stereoisomers are computed at the CC level (CCSD(T)) to assess the validity of proposed rearrangement mechanisms. While corroborating prior experimental IR and NMR assignments, the results are also able to remedy the “speculative” Raman and NMR assignments that lacked reliable computed values when the experiments were done. More importantly, the results identify “spectral fingerprints” that could distinguish various rotational isomers. These data, when used concurrently along with high resolution measurements, form a powerful basis for the characterization of various rotational isomers of PH_2F_3 . A “new” stability diagram and a rearrangement path based on the computed energetic and structure data are obtained. That is far superior to what has been available in the literature.

I. Introduction

Trifluorophosphorane, PH_2F_3 , and its intramolecular rearrangements have been widely studied during past decades by both experiment and theory as a classic prototype for pseudorotation. Variable temperature NMR experiments have shown that the molecule undergoes intramolecular rearrangements by exchanging the axial and the equatorial fluorines.¹ Different one step and multistep mechanisms have been proposed to explain these rearrangements. Electron diffraction measurements in the gas-phase established that the trifluorophosphorane (PH_2F_3) adopts a trigonal bipyramidal structure (TBP) with two fluorine atoms in axial positions, with the other three ligands occupying the equatorial positions (TBP1).²

The rearrangement mechanism has been the subject of great interest, especially since PH_2F_3 is a prototype of molecules that undergo permutational rearrangements. It has been shown that Berry's pseudorotation³ is more favored than the Turnstile rotation mechanism.⁴ Moreover, Strich has shown that the one-step mechanism for rearrangement is energetically unfavorable.⁵ The two multistep mechanisms corresponding to M_2 and M_4 (according to the nomenclature of Musher⁶ as depicted in Figure 1) consist of a succession of Berry's pseudorotations, which interconvert two TBP structures via a tetragonal pyramid (TP). On the basis of observations made by prior work,⁵ we conclude that the one-step mechanism is not energetically favorable, and choose not to consider that possibility further.

The first reported experimental study on phosphorane (PH_2F_3) by proton NMR was done by Holmes et al.⁷ However, Gilje and co-workers¹ were the first to suggest and study intramolecular rearrangements in PH_2F_3 by means of experimental and

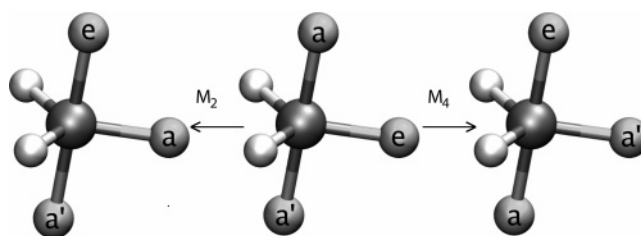


Figure 1. The two rearrangement modes, M_2 and M_4 , of PH_2F_3 .

theoretical ^1H variable temperature NMR spectroscopy. The first reported IR measurements were done by Treichel et al.,⁸ and in combination with mass spectral data, Treichel and co-workers attempted to correctly assign the vibrational modes of PH_2F_3 .⁸ In a follow up study using laser Raman spectroscopy, Holmes group⁹ completed the vibrational assignments of Treichel et al.⁸ by assigning the IR inactive bands. Christen et al.² determined the experimental geometry of PH_2F_3 and several other members of phosphorane family from gas-phase electron diffraction experiments. Most of the theoretical studies focused on the most stable isomer TBP1 of PH_2F_3 in the $\text{PH}_n\text{F}_{5-n}$ series and its vibrational modes, and relatively few focused on the intramolecular rearrangement mechanisms. Keil and Kutzelnigg¹⁰ published a study of the nature of the chemical bond in PH_2F_3 using estimated geometries from related fluorophosphoranes. Breidung et al.¹¹ computed the vibrational modes of TBP1 at the HF–SCF/6-31G** level and reevaluated the prior experimental assignments. Limited to small basis set Hartree–Fock self-consistent field method (HF–SCF), Strich considered the possible mechanisms of intramolecular rearrangements and

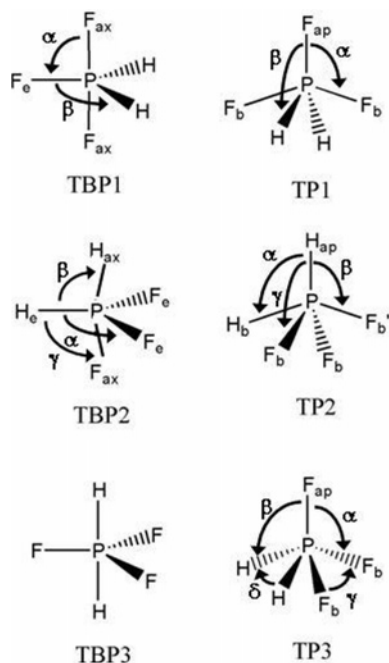


Figure 2. Illustration of the critical parameters and their labels of the six isomers of PH₂F₃.

concluded that the one-step mechanism was energetically unfavorable.⁵ The work of Wasada and Hirao has shown that perturbational methods such as MP2, MP3, and MP4 fail to describe the rearrangement path between TBP1, the transition state TP2, and TBP2¹² (see Figure 2). They found a small barrier at the SCF level of 0.13 kcal/mol between TBP2 and TP2, and a barrier of 12.03 kcal/mol between TBP1 and TBP2. These values are larger than those at the correlated level. In summary, it is apparent that the prior theoretical treatments are inadequate to differentiate small energy differences of PH₂F₃ isomers, and further refinement of the theoretical result for this “classic” problem using the state of the art theoretical methods is overdue.

To further elaborate, the structures, the energetics of the intermediates involved, the transition states that connect the intermediates, and the rearrangement mechanism are yet to be established by high level *ab initio* methods. Furthermore, the experimentally measured IR/Raman and NMR data have to be conclusively corroborated. Also, the investigation of the possibility of establishing spectroscopic fingerprints that differentiate rotational isomers for future experimental verification is equally important. To that end, this work employs predictive quality *ab initio* CC methods with various high-quality basis sets to obtain the relevant minima and transition state structures and energetics of the trifluorophosphorane isomers. A full array of spectroscopic data (IR/Raman frequencies and intensities and NMR shieldings and spin–spin coupling constants corresponding to the minimas) are presented, and a new stability diagram and rearrangement path between different structures is proposed.

II. Computational Details

The stereoisomers of PH₂F₃ participating in the multistep mechanism determined by Strich⁵ constitute three trigonal bipyramids, TBP1 (*C*_{2v}), TBP2 (*C*_s), and TBP3 (*D*_{3h}), and three tetragonal pyramids, TP1 (*C*_{2v}), TP2 (*C*_s), and TP3 (*C*_s) (see Figure 2), and form the basis for this work.

The equilibrium structures and harmonic vibrational frequencies are obtained at the coupled cluster singles and doubles (CCSD) level augmented by perturbative corrections for the connected triple excitations (CCSD(T)). The geometry optimiza-

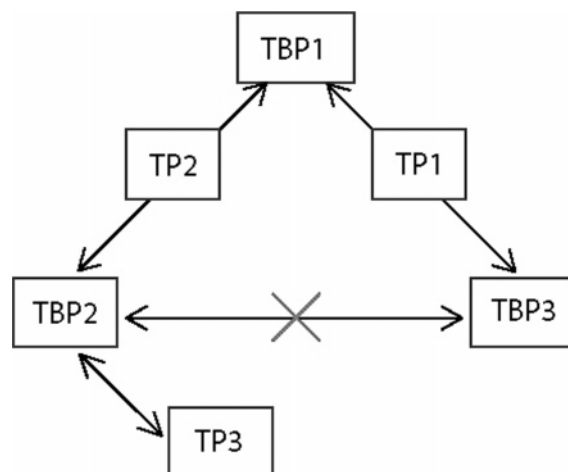


Figure 3. Possible arrangements among stable isomers and the transition states. There is no pathway between TBP2 and TBP3.

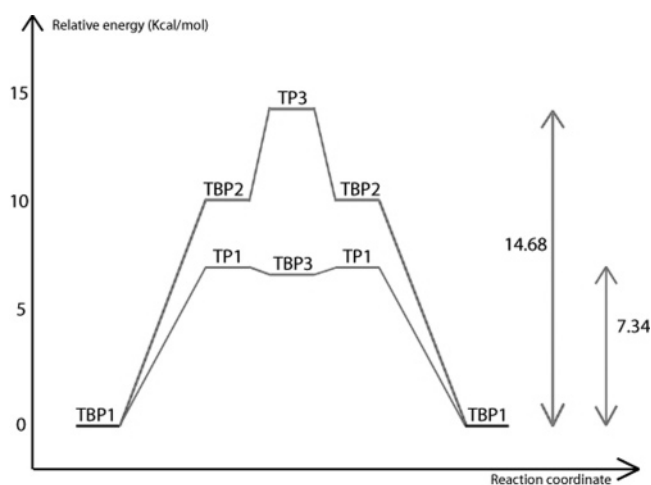


Figure 4. Relative stabilities of each isomers through M₂ (14.68 kcal mol⁻¹) and M₄ (7.34 kcal mol⁻¹) modes at the CCSD(T)/aug-cc-pVQZ level using CCSD(T)/aug-cc-pVTZ geometries.

tions are performed by analytical gradients combined with a classical Newton Raphson search algorithm guided by Hessian updates. The transition states are obtained using an *eigenvector following* algorithm.¹³ The Raman intensities, NMR shielding and NMR spin–spin coupling constants are computed at the CCSD, CCSD(T), and EOM-CCSD levels, respectively. The ACES II program system in its UF¹⁴ and MAB¹⁵ versions are used for all the computations.

Correlation consistent basis sets, namely cc-pVDZ, cc-pVTZ, and aug-cc-pVTZ basis sets^{16,17} are used for geometry optimizations, vibrational, and NMR shielding constant (cc-pVTZ only) calculations. The aug-cc-pVQZ basis sets are also used to perform single point energy calculations. The NMR spin–spin coupling constants are obtained with Ahlrichs qz2p basis sets.¹⁸ Our experience from numerous previous studies is that the Ahlrichs basis sets outperform other similarly sized basis sets for NMR spin–spin coupling constants. Other specialized basis sets used in this study are the Sadlej’s polarized basis sets^{19,20} for Raman intensity calculations. For further explanations of various choices of basis sets, see the Results and Discussion section below or the citations that are quoted. A description of the various basis sets used is shown in Table 1. The core orbitals were frozen and the spherical harmonic atomic orbital (AO) basis was used for all the geometry optimizations and energy and frequency calculations while all electron Cartesian AO basis was used for Raman and NMR calculations.

TABLE 1: Description of the Basis Sets Used in This Work and the Contraction Scheme: Primitives/Contracted^a

atom label	Ahlrichs ¹⁸	Sadlej ^{19,20}	cc-pVDZ ^{16,17}	cc-pVTZ ^{16,17}	aug-cc-pVTZ ^{16,17}
P	15s12p2d/10s7p2d	14s10p4d/7s5d2d	12s8p1d/4s3p1d	15s9p2d1f/5s4p3d1f	16s10p3d2f/6s5p3d2f
F	11s7p2d/6s4p2d	10s6p4d/5s3p2d	9s4p1d/3s2p1d	10s5p2d1f/4s3p2d1f	11s6p3d2f/5s4p3d2f
H	7s2p/4s2p	6s4p/3s2p	4s1p/2s1p	5s2p1d/3s2p1d	6s3p2d/4s3p2d

^a The core orbitals were frozen and a spherical harmonic AO Basis was used for all geometry, energy and frequency calculations while an all electron Cartesian AO basis was used for Raman and NMR calculations.

TABLE 2: Optimized Geometries with Bond Lengths and Bond Angles Given in Angstroms and Degrees, Respectively

isomer	symmetry	optimized parameters	RHF ⁵	CCSD(T)		
				cc-pVDZ	cc-pVTZ	aug-cc-pVTZ
TBP1	C_{2v}	PF _{ax}	1.610	1.659	1.624	1.632
		PF _e	1.562	1.605	1.558	1.561
		PH	1.368	1.401	1.388	1.389
		α	90.6	91.0	91.3	91.1
		β	117.5	116.8	116.8	116.8
TBP2	C_s	PF _{ax}	1.595		1.602	1.605
		PF _e	1.562		1.579	1.590
		PH _{ax}	1.368		1.413	1.412
		PH _e	1.384		1.398	1.396
		α	120.3		116.6	113.6
		β	90.0		94.9	97.0
		γ	90.0		91.7	93.4
TBP3	D_{3h}	PF	1.586	1.631	1.590	1.597
		PH	1.378	1.411	1.395	1.396
TP1	C_{2v}	PF _{ap}	1.579	1.617	1.572	1.579
		PF _b	1.594	1.639	1.601	1.608
		PH	1.375	1.410	1.395	1.395
		α	111.2	113.8	112.6	113.2
		β	98.3	93.4	94.3	94.0
TP3	C_s	PF _{ap}	1.548	1.592	1.552	1.555
		PF _b	1.594	1.640	1.598	1.605
		PH	1.392	1.423	1.414	1.415
		α	100.0	101.8	102.0	102.3
		β	105.1	101.6	101.6	101.4
		γ	86.2	88.4	89.1	88.6
		δ	92.7	95.6	94.9	95.7

^a Fixed parameters.

III. Results and Discussion

In this section, we discuss the structures of the six isomers obtained at different levels of theory using different basis sets, their relative stabilities, the intramolecular rearrangement mode that is most favored, and the spectroscopic data of structures corresponding to the minima (TBP1, TBP2, and TBP3).

A. Geometries. The optimized structures of the six stereoisomers of PH₂F₃ are depicted in Figure 2, and the corresponding optimized parameters are reported in Table 2 with results from previous calculations. The TBP1 structure is the most energetically favored, and TBP2 and TBP3 are isomers with one or both hydrogen atoms in axial positions, respectively. The local minimum corresponding to the TBP2 structure is located in a very shallow region of the potential energy surface. As a consequence, the geometry optimization must be tightly controlled to converge to the TBP2 structure. Failure to do so will result in converging to the TBP1 structure. TP1 is the transition state between TBP1 and TBP3, TP2 is the transition state between TBP1 and TBP2, and TP3 is the transition state between two TBP2 structures (two TBP2 structures are shown in Figure 5). The TP2 transition state is located in the proximity of the shallow TBP2 local minimum. Nature of that region of the PES is such that it is not possible to uniquely identify a structure corresponding to the TP2 transition state. Hence, we choose not to report a structure corresponding to TP2. As can

be inferred from Figures 3 and 5, there are no possible Berry pseudorotations between TBP2 and TBP3.

The TBP1 structure, the most stable form of PH₂F₃, is compared with experimental data in Table 3. Both CCSD(T)/cc-pVTZ and CCSD(T)/aug-cc-pVTZ geometries of TBP1 are in close agreement with experiment. In both cases, bond lengths are shorter than the values with the cc-pVDZ basis set. This trend is common for improvements in basis set quality. In contrast, however, the aug-cc-pVTZ bond lengths are slightly longer than the cc-pVTZ values. Bond angles are less affected by the basis set quality. Both cc-pVTZ and aug-cc-pVTZ computed bond lengths are longer than the experimental values, and the former shows better agreement with experiment. This has to be viewed with caution, since the experimental geometries of Christen et al.² are derived from microwave spectra using a rigid-rotor approximation, and for molecules like PH₂F₃ that undergo fast rearrangements, such an approximation might yield bond lengths that are shorter than the actual values. The computed geometry from Breidung and co-workers also agrees very well with experiment.¹¹ This agreement could be from an unexpected error cancellation, since their calculations are limited (HF-SCF with small 6-31G** basis set).

For each isomer (TBP1, TBP2, and TBP3) and transition state (TP1, TP2, and TP3), the same parameters (bond lengths and bond angles) are optimized as Strich⁵ with one exception and concerning TP1: Strich was unable to locate the transition state

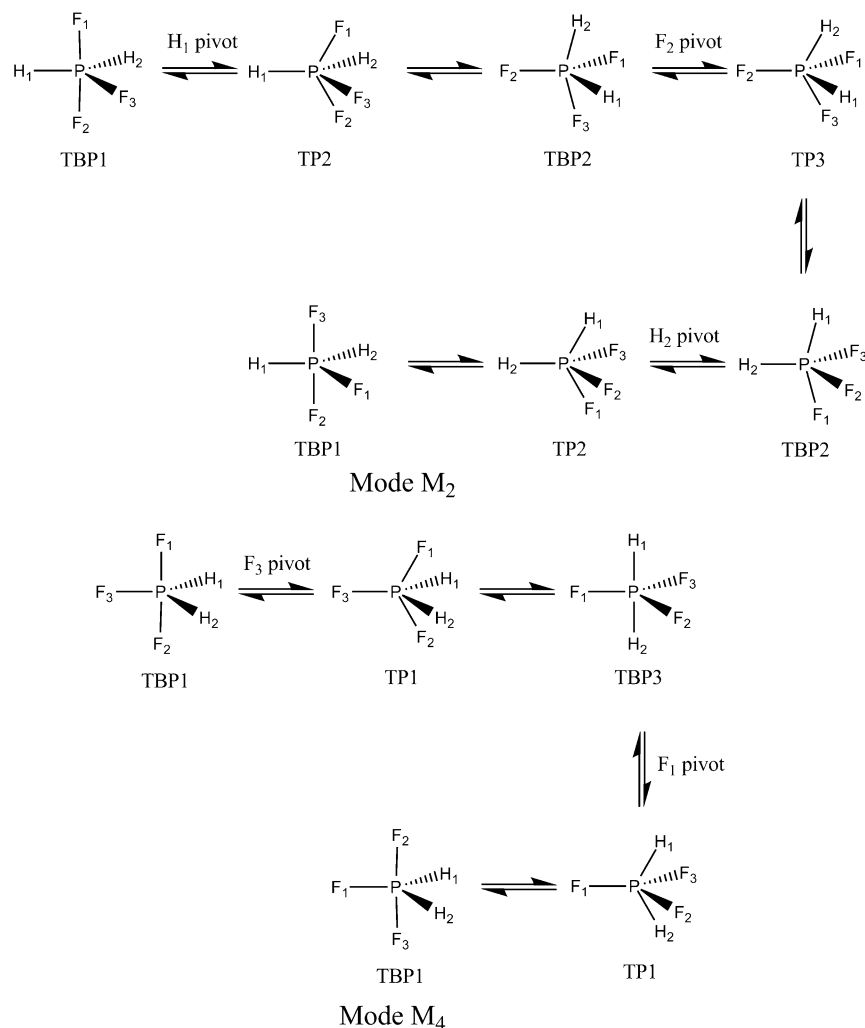


Figure 5. M_2 and M_4 modes described in detail.

TABLE 3: Comparison of Experimental and Calculated Geometries of the TBP1 Isomer Where Bond Lengths and Bond Angles Are Given in Angstroms and Degrees, Respectively

	RHF ⁵	RHF ¹¹	CCSD(T) cc-pVDZ	CCSD(T) cc-pVTZ	CCSD(T) aug-cc-pVTZ	expt ²
PF _a	1.610	1.611	1.659	1.624	1.632	1.618
PF _c	1.562	1.553	1.605	1.558	1.560	1.539
PH	1.368	1.373	1.401	1.388	1.389	1.375
α	90.6	90.4	91.0	91.3	91.1	91.9
β	117.5	117.4	116.8	116.8	116.8	117.1

connecting TBP1 and TBP3 and extrapolated its structure by calculating points on the reaction path connecting the two TBP structures. Our geometries for various isomers are similar to the HF geometries obtained by Strich with limited basis set showing once again that the small basis set HF calculations benefit from error cancellation.

B. Relative Stability of the Stereoisomers. The relative stabilities of each structure calculated at the CCSD(T)/cc-pVTZ and CCSD(T)/aug-cc-pVTZ levels are reported in Table 4 together with the previous results. The relative stabilities obtained at the CCSD(T)/aug-cc-pVQZ using CCSD(T)/aug-cc-pVTZ geometries are also presented. The TBP1 structure is the most stable. The TBP2 and TBP3 structures are 9.98 and 7.09 kcal mol⁻¹ higher respectively. The TBP2 is less stable than TBP3 except at the CCSD(T)/cc-pVTZ level. The order

of stability of the structures (TBP1 < TBP3 < TBP2) is in agreement with previous calculations of Strich where TBP3 was found to be more stable than TBP2. This order of stability does not follow the order of stability one would have obtained by applying the empirical rule which states that the most stable structure corresponds to the one where the greatest number of electronegative atoms are in axial positions.^{21,22}

In order to easily follow the points that we make in the preceding discussion, the reader is referred to Figures 3–5. The stereoisomer with the highest energy relative to TBP1 is TP3 (14.68 kcal mol⁻¹). This transition state plays a role in the M_2 mode interconverting a TBP2 into another TBP2 structure. Since TBP2 is 10.60 kcal mol⁻¹ above TBP1, the barrier between the two TBP2 structures is about 4 kcal mol⁻¹. The TP1 structure, which is the transition state between TBP1 and TBP3 is found 7.34 kcal mol⁻¹ above TBP1. In the M_2 mode, which interconverts two TBP1 structures, there is no barrier between TBP1 and TBP2, but the two TBP2 forms are separated by a 4 kcal mol⁻¹ barrier with transition state TP3. In the M_4 mode, starting from TBP1, the isomer TBP3 is obtained by a Berry pseudorotation where TP1 is the transition state connecting the two forms. From this geometry, a second Berry pseudorotation converts TBP3 to the final TBP1 structure. Starting and final TBP1 structures differ from each other by an exchange of the three fluorine atoms. The activation barrier of

TABLE 4: Energies and Relative Stabilities of the Isomers at the CCSD(T)/cc-pVTZ and CCSD(T)/aug-cc-pVTZ Levels^a

isomers	RHF ⁵		CCSD(T)/cc-pVTZ		CCSD(T)/aug-cc-pVTZ		CCSD(T)/aug-cc-pVQZ ^b	
	energy (au)	stability	energy (au)	stability	energy (au)	stability	energy (au)	stability
TBP1	-640.0816	0.0	-641.3930	0.0	-641.4287	0.0	-641.5305	0.0
TBP2	-640.0625	12.0	-641.3767	10.23	-641.4124	10.23	-641.5146	9.98
TBP3	-640.0667	9.31	-641.3820	6.95	-641.4167	7.55	-641.5192	7.09
TP1	-640.0654	10.2	-641.3815	7.24	-641.4163	7.79	-641.5188	7.34
TP3	-640.0546	16.9	-641.3704	14.18	-641.4046	15.12	-641.5071	14.68

^a The stabilities relative to TBP1 are given in kcal mol⁻¹. ^b CCSD(T)/aug-cc-pVQZ single point energies are computed at the CCSD(T)/aug-cc-pVTZ optimized geometries.

TABLE 5: Harmonic Vibrational Frequencies of TBP1 at the CCSD(T) Level^a

normal mode	symmetry	RHF ¹¹	cc-pVDZ	cc-pVTZ	exptl ⁸	assignment ν_1
ν_1	A ₁	2767 (33)	2561 (18)	2561 (18)	2482 (m)	s-stretch eq.
ν_2	A ₁	1118 (236)	987 (189)	1014 (179)	1005 (vs)	scissors eq.
ν_3	A ₁	945 (27)	833 (10)	872 (14)	864 (m)	PF stretch
ν_4	A ₁	698 (1)	653 (1)	649 (2)	614 (w)	s-stretch ax.
ν_5	A ₁	351 (20)	301 (16)	315 (16)	335 (m)	s-bending ax.
ν_6	A ₂	1361 (-)	1222 (-)	1269 (-)	1233 (-)	PH ₂ wag.
ν_7	B ₁	2812 (79)	2618 (52)	2612 (46)	2549 (m)	a-stretch eq.
ν_8	B ₁	844 (119)	735 (88)	766 (83)	767 (s)	PH ₂ rock. eq.
ν_9	B ₁	354 (28)	333 (22)	349 (22)	308 (w)	a-bending ax.
ν_{10}	B ₂	1443 (46)	1285 (37)	1323 (12)	1291 (w)	PH ₂ deform.
ν_{11}	B ₂	957 (525)	903 (423)	871 (443)	825 (vs)	a-stretch. ax.
ν_{12}	B ₂	503 (10)	442 (10)	474 (10)	472 (m)	PF deform

^aFrequencies are given in cm⁻¹ and intensities are given in parentheses in km/mol. The relative experimental intensities are given in parentheses with labels vs = very strong, s = strong, m = medium, w = weak, vw = very weak, and - = forbidden.

the M₄ mode is then the energy of TP1 relative to TBP1 which is 7.34 kcal/mol.

The energy difference of 0.25 kcal/mol between TP1 and TBP3 structures suggests that the TBP3 structure is metastable. This result disagrees with the results of Wasada and Hirao.¹² They found that TP1 is more stable than TBP3 by a few tenths of a calorie per mole at the MP2, MP3, MP4(DQ), MP4(SDQ), MP4(SDTQ), SDCI, and SDCI levels with Davidson's correction using a DZP basis set and SCF-optimized geometries, but such differences are well below the inherent error in the calculation. However, they concluded that the Berry pseudorotation is not a possible mechanism to explain the intramolecular rearrangement and that the correlation energy is important but not essential. Our calculations dispute Wasada and Hirao's conclusions since, as we have shown, a better method (CCSD(T)) with flexible basis sets leads to different conclusions. It is important to note that all our structures are optimized at the CCSD(T) level of theory. The difference between the two activation barriers of the modes M₂ and M₄ are 14.68 and 7.34 kcal/mol, respectively, which show that the most favorable intramolecular rearrangement of axial and equatorial fluorine atoms is the M₄ mode. This observation is in qualitative agreement with the previous work of Strich, but the barrier height here is far more quantitative.

C. Harmonic Vibrational Frequencies and Intensities. The theoretical double harmonic vibrational spectrum (IR and Raman) of TBP1 and TBP3 are obtained as a function of increasing basis set quality. The CCSD(T)/aug-cc-pVTZ IR frequencies and intensities are presented in Table 4 along with the previous data and experimental data. Each theoretical study use the optimized CCSD(T) geometry obtained with the corresponding basis set. The Raman intensity calculations are currently limited to CCSD, and they are shown in Table 6 along with the corresponding IR frequencies and intensities. The IR and Raman modes are complementary to each other: IR inactive vibrations are Raman active and vice versa. The computed frequencies are in good agreement with the experimental values. The experimental work⁹ was done a few decades ago and was

subjected to the technical limitations of IR instruments at the time. Hence, new high-resolution experiments are needed to assess our predicted results. Also, the issue of anharmonicity should be considered in improved theory prediction.

Improving the quality of the basis set and the accuracy of the optimized geometry lead to better agreement with experiment. The largest deviation from experiment is only 79 cm⁻¹ for the ν_1 mode at the CCSD(T)/cc-pVTZ level (see Table 5). Each mode can be clearly assigned by using symmetry, the intensities, and the nuclear displacements. Except for qualitative labels such as strong, medium and weak, no quantitative experimental IR or Raman intensities are available in the literature. However, if we roughly assume that the computed intensities in the range 10–20 km/mol as medium, above 20–100 km/mol as strong, and above 100 km/mol as very strong, then the computed intensities reproduce observed qualitative assignments except for the ν_9 and ν_{10} modes which are identified as weak absorptions from experiment, and they should be of medium strength based on a theoretical standpoint.

Purely from a theoretical viewpoint, it would be more interesting to look at how intensities change with improvements in theory and basis sets and to make comparisons to previous theoretical studies. For example, the intensity of the ν_{10} mode is overestimated by the RHF/6-31G**, and CCSD(T)/cc-pVTZ brings this into agreement with relatively weak intensity in the experimental spectrum. The first theoretical assessment of the experimental vibrational assignments were reported by Breidung and co-workers.¹¹ Despite the fact that analysis of the results, their SCF/6-31G** calculations are modest according to current standards, our independent analysis with the results obtained from high level theoretical methods confirm their analysis of the experimental observations. In particular, Breidung and co-workers argued that the dipole-forbidden a₂ ν_6 mode must be assigned to the Raman band at 1233 cm⁻¹, which was originally assigned experimentally as the a₁ ν_2 mode by Holmes and Hora.⁹ Nevertheless, without theoretical Raman intensities to support either arguments, the true nature of this band had remained inconclusive. With the present Raman intensities, we are now

TABLE 6: CCSD/aug-cc-pVTZ and CCSD/PBS IR/Raman Frequencies and Intensities Obtained at the CCSD(T)/cc-pVTZ and CCSD(T)/PBS Geometries, Respectively^a

		TBP1											
		ν	ν_2	ν_3	ν_4	ν_5	ν_6	ν_7	ν_8	ν_9	ν_{10}	ν_{11}	ν_{12}
		(A ₁)	(A ₂)	(B ₁)	(B ₁)	(B ₁)	(B ₂)	(B ₂)	(B ₂)				
		Sadlej											
IR	2594	997	857	673	303	1224	2653	707	310	1275	918	457	
	(13)	(182)	(3)	(2)	(15)	(0)	(28)	(79)	(16)	(1)	(468)	(12)	
Raman	159	5	7	7	0.2	6	25	2	0.5	2	0	0.7	
	(0.07)	(0.0)	(0.55)	(0.25)	(0.63)	(0.75)	(0.75)	(0.75)	(0.75)	(0.75)	(0.75)	(0.75)	(0.75)
		aug-cc-pVTZ											
IR	2547	1012	874	644	324	1282	2593	781	369	1326	855	473	
	(14)	(164)	(24)	(2)	(18)	(0)	(30)	(74)	(26)	(8)	(475)	(10)	
Raman	157	3	7	6	0.1	5	22	2	0.3	1	0	0.6	
	(0.07)	(0.17)	(0.30)	(0.23)	(0.66)	(0.75)	(0.75)	(0.75)	(0.75)	(0.75)	(0.75)	(0.75)	(0.75)
		TBP3											
		ν_1	ν_2	ν_3	ν_4	ν_5	ν_6	ν_7	ν_8	ν_9	ν_{10}	ν_{11}	ν_{12}
		A ₁)	(A ₁)	(A ₁)	(A ₁)	(A ₁)	(A ₁)	(A ₁)	(A ₁)	(A ₁)	(A ₁)	(A ₁)	(A ₁)
		Sadlej											
IR	2497	2428	1182	1182	1137	1137	839	839	632	580	101	101	
	(76)	(0)	(31)	(31)	(0)	(0)	(362)	(362)	(0)	(143)	(3)	(3)	
Raman	0.0	182	0.31	0.61	1.33	30	5.9	2.5	11.5	0.0	2.4	0.06	
	(0.75)	(0.13)	(0.75)	(0.75)	(0.75)	(0.75)	(0.75)	(0.75)	(0.09)	(0.75)	(0.75)	(0.75)	(0.75)
		aug-cc-pVTZ											
IR	2573	2482	1311	1311	1229	1229	904	904	686	615	144	144	
	(136)	(0)	(52)	(52)	(0)	(0)	(344)	(344)	(0)	(152)	(3)	(3)	
Raman	0.0	168	0.13	0.17	10.9	12.5	5.4	1.1	8.5	0.0	2.0	0.13	
	(0.75)	(0.11)	(0.75)	(0.75)	(0.75)	(0.75)	(0.75)	(0.75)	(0.10)	(0.75)	(0.75)	(0.75)	(0.75)

^a The IR frequencies are given in cm⁻¹ and the intensities given in parentheses in km/mol. The Raman intensities are in A₄/amu (amu = atomic mass unit) and the depolarization ratios are in parentheses. The polarizability derivatives (related to Raman intensities) are computed by numerically differentiating analytically computed polarizabilities. As result of the shallow nature of the TBP2 minimum, the numerical differentiation is subjected to large uncertainties. Hence, the Raman intensities for the TBP2 structure are not computed.

in a position to conclusively assign this mode. However, before we proceed to do that, some general remarks about the Raman intensity computations are warranted.

Raman intensities are related to the polarizability derivatives, and as polarizabilities are second-order properties (a response to an external electric field), they depend upon more quantities than an energy evaluation does.^{23,24} Therefore, the basis set must be flexible enough to describe both ground and excited states well enough to handle the polarizabilities. It is not yet well established in the literature which basis sets can perform well in both of these scenarios.²³ So, we have chosen to use cc-pVTZ and aug-cc-pVTZ to be consistent with the rest of the work, but we also considered the specially designed basis set for electrical properties developed by Sadlej.^{19,20} We observed that the deviation of Raman intensities among three basis sets is negligible and show only the aug-cc-pVTZ and Sadlej basis set results in Table 6. Two noteworthy features of the TBP1 Raman Spectra are the very strongly Raman active ν_1 band and the IR forbidden ν_6 band. Strongly Raman active and IR forbidden ν_6 (A₁ symmetry) frequency at 1229 cm⁻¹, two Raman inactive and strongly IR active ν_1 (2573 cm⁻¹, A₁ symmetry) and ν_{10} (615 cm⁻¹, A₁ symmetry), and IR inactive and Raman active ν_2 (2482 cm⁻¹, A₁ symmetry) and ν_9 (686 cm⁻¹, A₁ symmetry) in TBP3 are also noteworthy.

Despite the fact that the computed Raman intensity of the ν_6 band of TBP1 indicates that it is relatively weak, it is the only IR inactive band in both computed and observed frequency range of 1000–1500 cm⁻¹ and that has a₂ character. The only other band in that range is ν_2 , and it is strongly IR active with an a₁ character. At this point it is important to point out that the TBP3 form has strong Raman active band in the same frequency range, and it is possible that the strong Raman intensity seen in the

experiment may have been influenced by the presence of the TBP3 form. On the basis of these observations, we conclude that Holmes and Hora's original assignment of this band is erroneous. Another important observation is that the experimental frequency of this IR inactive band is actually determined from liquid or solid-state Raman spectroscopy,⁹ and according to them the most intense Raman bands are ν_3 and ν_4 . Our computed results indicate that the strongest Raman active bands are ν_1 and ν_7 . This apparent discrepancy can perhaps only be resolved by a new gas-phase Raman measurements with high-resolution Raman spectroscopy.

D. NMR Spectra. The computed NMR spin–spin coupling constants and the shielding constants for TBP1, TBP2, and TBP3 are shown in Table 7 along with three independent experimental NMR studies of proton (¹H) and fluorine (¹⁹F) coupling constants of PH₂F₃. The corresponding absolute shielding constants are shown in Table 8. No experimental shielding data is given since in order to convert experimental chemical shifts to absolute shieldings requires NMR shielding calculation of several different reference molecules. Since our primary interest is the relative shielding among the three isomers, we have not attempted to compute chemical shifts (or convert experimental data to absolute shieldings) in this work, but this is addressed in our future work where we plan to establish an absolute scale for NMR shifts.²⁵ The experimental spin–spin coupling constants data from all three are arranged in chronological order and are from Holmes and Storey,⁹ Gilje et al.,¹ and Treichel et al.,⁸ respectively.

The NMR spin–spin coupling tensor is a sum of four contributions: the Fermi contact (FC), spin–dipole (SD), paramagnetic spin–orbit (PSO), and diamagnetic spin–orbit (DSO). It is evident from our results in Table 7 that all four

TABLE 7: NMR Spin–Spin Coupling Constants of TBP1, TBP2, and TBP3 (in Hz), Where the CCSD(T)/cc-pVTZ Geometries Were Used

	coupling	PSO	DSO	FC	SD	total	expt	
TBP1	$^1J(\text{PF}_e)$	−145.3	1.0	−809.7	28.7	−925.3	770, ^a 877 ^b	
	$^1J(\text{PF}_{\text{ax}})$	−91.1	0.9	−721.5	27.3	−784.4		
	$^2J(\text{F}_{\text{ax}}\text{F}_{\text{ax}})$	−15.8	−3.5	116.0	−1.4	95.3		
	$^2J(\text{F}_e\text{F}_{\text{ax}})$	−89.2	−0.3	41.8	37.8	−9.9		
	$^2J(\text{HF}_e)$	0.5	−2.4	30.6	−0.6	28.1		
	$^2J(\text{HF}_{\text{ax}})$	−4.7	0.0	108.5	−1.0	102.8		
	$^1J(\text{PH})$	−2.0	1.4	754.4	−1.0	752.8		63, ^a 80, ^b 105 ^c
	$^2J(\text{HH})$	2.0	−4.1	15.7	0.0	13.6		908, ^a 825, ^b 865 ^c
	$^1J(\text{PF}_e)$	−135.9	1.0	−888.4	27.1	−996.2		34 ^c
	$^1J(\text{PF}_{\text{ax}})$	−109.9	1.0	−764.6	21.2	−852.3		
TBP2	$^2J(\text{F}_e\text{F}_e)$	92.9	−2.4	20.4	5.5	116.4		
	$^2J(\text{F}_e\text{F}_{\text{ax}})$	−177.5	−0.1	98.1	24.5	−55.0		
	$^2J(\text{H}_{\text{ax}}\text{F}_{\text{ax}})$	2.0	−4.9	10.6	−0.1	7.6		
	$^2J(\text{H}_{\text{ax}}\text{F}_e)$	−3.4	0.1	173.0	−1.4	168.3		
	$^1J(\text{PH}_{\text{ax}})$	−2.3	1.3	574.0	−0.5	572.5		
	$^2J(\text{H}_{\text{ax}}\text{H}_e)$	0.2	−0.5	42.2	0.2	42.1		
	$^1J(\text{PH}_e)$	−2.4	1.3	610.0	−0.1	608.8		
	$^2J(\text{H}_e\text{F}_e)$	1.0	−2.4	−2.5	−0.3	−4.2		
	$^2J(\text{H}_e\text{F}_{\text{ax}})$	−4.0	−0.2	128.9	−1.1	123.6		
	$^1J(\text{PF})$	−146.6	0.9	−1065.5	29.5	−1181.7		
TBP3	$^2J(\text{FF})$	111.9	−2.0	60.9	7.6	178.4		
	$^2J(\text{FH})$	−4.4	0.0	175.9	−1.4	170.1		
	$^1J(\text{PH})$	−2.3	1.4	850.7	−0.6	849.2		
	$^2J(\text{HH})$	3.4	−6.8	0.4	0.3	−2.7		

^a From ref 7. ^b From ref 8. ^c From ref 1.

TABLE 8: CCSD(T)/cc-pVTZ NMR Absolute Shieldings in ppm

	P	F _{ax}	F _e	H _{ax}	H _e
TBP1	358	218	312		25
TBP2	416	253	273	25	26
TBP3	348		229	25	

contributions must be computed in order to be accurate and to have predictive quality. The widely used assumption that except for the FC term the other three contributions are negligible does not apply here. The equation-of-motion of coupled cluster method (EOM-CCSD) used here, was developed by Perera and Bartlett^{26,27} has been shown to be able reproduce experimental results to ± 5 Hz accuracy irrespective of the atoms involved in coupling. The NMR absolute shielding constants, which can be easily converted to the shift scale using the reference shieldings, are computed at the CCSD(T) level using gauge-including atomic orbitals (GIAO).^{28–30} The use of GIAOs rigorously eliminates the gauge origin dependent error of finite basis set NMR shift calculations. Lack of rigorous gauge invariance often leads to degradation of accuracy and reproducibility. Moreover, both NMR spin–spin coupling constants and chemical shifts have large electron correlation contributions and are strongly affected by the basis set quality. A detailed discussion of these and other aspects of NMR calculations is not within the context of this work, and hence an interested reader is referred to elsewhere. Nevertheless, it must be emphasized that in this study all these factors required to properly compute NMR data that can be compared to experiments or can aid in interpreting NMR spectra are included.

The use of NMR spin–spin coupling constants as a primary tool in conformational analysis, which is a consequence of their sensitivity to relative nuclei position, can be easily demonstrated from the data shown in Table 7 for TBP1, TBP2, and TBP3. It is not only the number of distinct couplings constants, which is a result of the different numbers of magnetically equivalent atoms in the three forms, but also the significantly different individual couplings constants that make the NMR spin–spin

couplings constants a unique tool in conformational analysis. For example, $^1J(\text{PF}_{\text{ax}})$ in TBP1 is -784 Hz while in TBP2 it is -852 Hz, and similar data are observed for $^2J(\text{HH})$, $^2J(\text{HF})$, and, to a lesser degree, for $^1J(\text{PH})$. For discussion purposes, we choose generic labels to identify the coupling constants instead of identifying them with proper subscripts as shown in Table 7. Also, the $J(\text{PF}_e)$ is -925 , -996 , and -1181 Hz respectively for the three isomers. These are the spectral fingerprints that a predictive theory can provide so that when experimental measurements are made, the association of the structure with the spectra becomes relatively easy. This is of course very relevant if the structures differ only by permutational symmetry as is the case here. We also give the NMR shielding data computed at the CCSD(T)/cc-pVTZ level. Since the only difference between TBP1, TBP2 and TBP3 is permutational symmetry, they are not expected to show substantial differences in shielding constants. Nevertheless, as evident from Table 8, the shielding data can also be potentially important in distinguishing the three structures of TBP1, TBP2, and TBP3. Except for the proton, we observe that the absolute shielding of other nuclei show substantial differences depending on their arrangement as in the TBP1, TBP2, or TBP3 forms! Due to the high point group symmetry (D_{3h}) TBP3 isomer has fewer unique coupling constants. The individual coupling constants seem to be much closer to the TBP2 form than TBP1. This is expected as TBP2 and TBP3 forms share more structural similarities; both forms have at least a one axial proton and two equatorial fluorines. In the context of conformational analysis it is interesting to see how the coupling constants vary as the atoms change their positions from axial to equatorial (or vice versa). For example, the $J(\text{HH})$ changes from $+14$ to $+42$ and to -3 Hz as the proton changes from both being equatorial in TBP1, one being axial and one equatorial in TBP2, and both being axial in TBP3. A similar observation can be made for $J(\text{PF})$ too! Just as it was the case for spin–spin coupling constants,

the absolute shieldings of TBP3 show more similarities to TBP2, further confirming that they share similar chemical environments.

The three experiments differ from each other as a result of the experimental conditions such as the temperature and the nature of the sample. For example, Holmes and Storey⁹ used neat PH₂F₃ samples or solutions in inactive solvents at several different temperatures (the results quoted here correspond to the neat sample at the lowest temperature reported), while Treichel et al.⁸ made gas phase measurements. In the case of Gilje et al.¹ no details about the character of the sample are available. We can immediately notice that there are significant differences among the three experiments, but at the same time all three unambiguously assign the observed NMR to the TBP1 structure. The variations among different experiments are somewhat expected since the temperature and the character of the sample (neat vs dissolved in inactive solvents) are varied among them, and the differences in the environment, especially the temperature, can influence the NMR significantly for systems that can undergo internal rotations. Nevertheless, let us compare these values in conjunction with the computed values for TBP1, TBP2, and TBP3 structures, while noting that the computed values correspond to an isolated gas-phase molecule at 0 K. The largest measured and computed coupling constants are ¹J(PF) and ¹J(PH), and only the TBP1 has a computed ¹J(PH) coupling that qualitatively agrees with the measured values. Also, the statistical average -831.4 Hz of the computed values of ¹J(PF_{ax}) and ¹J(PF_e) of TBP1 is in much better agreement with the measured values than the similarly averaged -948 Hz ¹J(PF) coupling of TBP2. There is no uncertainty about the assignment of the observed ¹J(HF) values to TBP1 since there are no ¹J(HF) coupling constants for TBP2 or TBP3 that match the observed values. It is difficult to make a fair assessment about the observed ¹J(HH) coupling constant aside from saying that it is almost the average of the computed values for TBP1 and TBP2. While expected, it is important to mention that statistically averaged computed results show better agreement with the gas-phase results reported by Treichel et al.⁸ A new measurement of ²J(HH), preferably in the gas phase, would be useful to assess why the computed ²J(HH) fails to match the sole experimental result available for this coupling, since the nature of the sample that lead to the reported value is unspecified. The largest error we have seen for several ²J(HH) coupling constants is 2–3 Hz.³¹

The comparison of computed chemical shift data with available experimental data is less straightforward than the spin–spin coupling constants as a result of the different internal standards that are used to generate chemical shifts. That of course makes it harder to make comparison even between different experiments. We will provide absolute shieldings for all of the common reference molecules in a future paper to make it possible to readily compare relative shieldings with each other.²⁵

IV. Conclusions

The intramolecular rearrangement mechanisms of PH₂F₃, which is a prototype molecule that undergoes pseudorotations, has been studied using state-of-the-art coupled cluster theoretical methods and large basis sets to obtain results that are converged with respect to basis set and correlation effects. Unless otherwise stated, the geometries of the six stereoisomers were optimized at the same level of theory (CCSD(T)/aug-cc-pVTZ) and aug-cc-pVQZ single point energies were obtained at the optimized geometries to assess the relative stability of various isomers.

The optimized geometry of TBP1, the most stable isomer, is in good agreement with the experimental structure. The empirical rule favoring as many as possible electronegative atoms in axial position is not followed, the order of stability at the CCSD(T)/aug-cc-pVTZ level is TBP1 < TBP3 < TBP2.

The two possible modes of rearrangement, M₂ and M₄, have been characterized as transition states and metastable intermediates. The activation barrier of M₂ is 14.68 kcal/mol where the M₄ mode has an activation barrier of 7.34 kcal/mol at the CCSD(T)/aug-cc-pVQZ using CCSD(T)/aug-cc-pVTZ geometries. We show that mode M₄, exchanging the three fluorine atoms, is the most favorable one.

The computed harmonic vibrational (IR and Raman) frequencies as well as the intensities are in good agreement with experimental data (in the case of intensities qualitatively). We support the previous assignment of Breidung and co-workers. More importantly, with the aid of computed Raman intensities we are able to resolve the discrepancy between theory and experimental assignments of the IR inactive band. We have been able to verify the previous NMR assignments for the TBP1 structure, which we also identify as the energetically most favored form. The other most likely structures (TBP2 and TBP3 structures) shows a significantly different NMR signature, and we are able to identify fingerprints that can unambiguously distinguish the three forms.

Acknowledgment. The preliminary calculations of this work were carried out while A.S. was spending a sabbatical semester in the group of R.J.B. in 2002. A.S. thanks R.J.B. for his hospitality and for financial support. This work was undertaken as a part of a CNRS/NSF collaborative project (No. 17097) and a NSF Grant (Program No. 03-559). S.V. thanks the Ministère de l'Éducation Nationale, de l'Enseignement Supérieur et de la Recherche, and the Quantum Theory Project. The quantum chemical calculations were carried out either at the Quantum Theory Project (Gainesville, Florida) or at the Laboratoire de Chimie Quantique (Strasbourg, France).

References and Notes

- (1) Gilje, J. W.; Braun, R. W.; Cowley, A. H. *J. Chem. Soc., Chem. Commun.* **1974**, 15–17.
- (2) Christen, D.; Kadel, J.; Liedtke, A.; Minkwitz, R.; Oberhammer, H. *J. Phys. Chem.* **1989**, *93*, 6672–6675.
- (3) Berry, R. S. *J. Chem. Phys.* **1960**, *32*, 933–938.
- (4) Ugi, I.; Marquarding, D.; Klusacek, H.; Gillespie, P.; Ramirez, F. *Acc. Chem. Res.* **1971**, *4*, 288–296.
- (5) Strich, A. *Inorg. Chem.* **1978**, *17*, 942–947.
- (6) Musher, J. I. *J. Am. Chem. Soc.* **1972**, *94*, 5662–5665.
- (7) Holmes, R. R.; Storey, R. N. *Inorg. Chem.* **1966**, *5*, 2146–2151.
- (8) Treichel, P. M.; Goodrich, R. A.; Pierce, S. B. *J. Am. Chem. Soc.* **1967**, *89*, 2017–2022.
- (9) Holmes, R. R.; Hora, Jr., C. J. *Inorg. Chem.* **1972**, *11*, 2506–2515.
- (10) Keil, F.; Kutzelnigg, W. *J. Am. Chem. Soc.* **1975**, *97*, 3623–3632.
- (11) Breidung, J.; Thiel, W.; Komornicki, A. *J. Phys. Chem.* **1988**, *92*, 5603–5611.
- (12) Wasada, H.; Hirao, K. *J. Am. Chem. Soc.* **1992**, *114*, 16–27.
- (13) Cerjan, C. J.; Miller, W. H. *J. Chem. Phys.* **1981**, *75*, 2800–2806.
- (14) Stanton, J. F.; Gauss, J.; Perera, S. A.; Yau, A. D.; Watts, J. D.; Nooijen, M.; Oliphant, N.; Szalay, P. G.; Lauderdale, W. J.; Gwaltney, S. R.; Beck, S.; Balková, A.; Bernholdt, D. E.; Baeck, K.-K.; Rozyczko, P.; Sekino, H.; Huber, C.; Pittner, J.; Bartlett, R. J. ACES II is a program product of the Quantum Theory Project, University of Florida. Integral packages included are VMOL (J. Almlöf and P. R. Taylor); VPROPS (P. R. Taylor); ABACUS (T. Helgaker, H. J. Aa. Jensen, P. Jørgensen, J. Olsen, and P. R. Taylor).
- (15) Stanton, J. F.; Gauss, J.; Watts, J. D.; Szalay, P. G.; Bartlett, R. J. ACES II Austin-Mainz-Budapest version, a quantum chemical program package. 2005. Contribution from: Auer, A. A.; Bernholdt, D. B.; Christiansen, O.; Harding, M. E.; Heckert, M.; Heun, O.; Huber, C.; Jonsson, D.; Juselius, J.; Lauderdale, W. J.; Metzroth, T.; Ruud, K. Integral packages included are VMOL (J. Almlöf and P. R. Taylor); VPROPS (P. R. Taylor);

ABACUS (T. Helgaker, H. J. Aa. Jensen, P. Jørgensen, J. Olsen, and P. R. Taylor). See also: Stanton, J. F.; Gauss, J.; Watts, J. D.; Lauderdale, W. J.; Bartlett, R. J. *Int. J. Quantum Chem. Symp.* **1992**, 26, 879.

- (16) Dunning, Jr, T. H. *J. Chem. Phys.* **1989**, 90, 1007–1023.
(17) Woon, D. E.; Dunning, T. H., Jr. *J. Chem. Phys.* **1993**, 98, 1358–1371.
(18) Schäfer, A.; Horn, H.; Ahlrichs, R. *J. Chem. Phys.* **1992**, 97, 2571–2577.
(19) Sadlej, A. J. *Collect. Czech. Chem. Commun.* **1988**, 55, 1995–2016.
(20) Sadlej, A. J. *Theor. Chim. Acta* **1991**, 79, 123–140.
(21) Muettterties, E. L.; Mahler, W.; Schmutzler, R. *Inorg. Chem.* **1963**, 2, 613–618.
(22) Gillespie, R. J. *J. Chem. Educ.* **1970**, 47, 18–23.

- (23) Perera, S. A.; Bartlett, R. J. *Chem. Phys. Lett.* **1999**, 314, 381–387.
(24) Stanton, J. F.; Bartlett, R. J. *J. Chem. Phys.* **1999**, 98, 7029–7039.
(25) Perera, S. A.; Bartlett, R. J. To be published.
(26) Perera, S. A.; Sekino, H.; Bartlett, R. J. *J. Chem. Phys.* **1994**, 101, 2186–2191.
(27) Perera, S. A.; Nooijen, M.; Bartlett, R. J. *J. Chem. Phys.* **1996**, 104, 3290–3305.
(28) Gauss, J. *Chem. Phys. Lett.* **1992**, 191, 614–620.
(29) Gauss, J. *J. Chem. Phys.* **1993**, 99, 3629–3643.
(30) Auer, A. A.; Gauss, J.; Stanton, J. F. *J. Chem. Phys.* **2003**, 118, 10407–10417.
(31) Perera, S. A.; Bartlett, R. J. *Magn. Reson. Chem.* **2001**, 39, S183–S189.